JOURNAL OF GEOPHYSICAL RESEARCH, VOL. 108, NO. A9, 1354, doi:10.1029/2002JA009777, 2003

A tilted-dipole MHD model of the solar corona and solar wind

A. V. Usmanov[1] and M. L. Goldstein
NASA Goddard Space Flight Center, Greenbelt, Maryland, USA

Received 12 November 2002; revised 18 March 2003; accepted 22 July 2003; published 30 September 2003.

[1] We simulate the three-dimensional structure of the heliosphere during solar activity minimum by specifying boundary conditions at the coronal base. We compare the output of the model with Ulysses observations obtained during the spacecraft's first fast latitude transition in 1994–1995. The polytropic MHD equations are solved for a steady coronal outflow that includes the addition of Alfvén wave momentum and energy in the WKB approximation. A solution for the outflow in a tilted dipole magnetic field in the inner computational region (1–20 $R_\odot$) is combined with a three-dimensional solution in the outer region which extends to 10 AU. The inner region solution is essentially the same as in the work of *Usmanov et al.* [2000] but has been obtained for slightly different boundary conditions using a different numerical algorithm. The dipole orientation is chosen to match the one inferred from photospheric magnetic field observations at the Wilcox Solar Observatory. The steady solution in the outer region is constructed using a marching-along-radius method and models both solar rotation and interaction regions. The bimodality of solar wind with a rapid change in flow parameters with latitude and the observed extent of the slower wind belt are reproduced well. We compare our simulation also with the results of *Bruno et al.* [1986] and empirical models of coronal density. We show that the simulation results are in good agreement with the empirical model of *Wang and Sheeley* [1990]. *INDEX TERMS:* 2134 Interplanetary Physics: Interplanetary magnetic fields; 2102 Interplanetary Physics: Corotating streams; 2169 Interplanetary Physics: Sources of the solar wind; 7536 Solar Physics, Astrophysics, and Astronomy: Solar activity cycle (2162); *KEYWORDS:* solar wind structure, solar wind sources, coronal holes, MHD simulation, Ulysses, Wang-Sheeley model

Citation: Usmanov, A. V., and M. L. Goldstein, A tilted-dipole MHD model of the solar corona and solar wind, *J. Geophys. Res.*, *108*(A9), 1354, doi:10.1029/2002JA009777, 2003.

1. Introduction

[2] During its first fast latitude scan in 1994–1995, Ulysses revealed a bimodal solar wind with a sharp transition from a relatively uniform fast and tenuous wind at high latitudes to a slower and denser wind near the solar equator [*Phillips et al.*, 1995]. The magnetic field was dominantly outward in the Northern Hemisphere and inward in the Southern Hemisphere and showed no prominent dependence on latitude in the fast wind [*Balogh et al.*, 1995; *Forsyth et al.*, 1996]. The Ulysses observations were taken just prior to solar activity minimum when the dominant component of the solar magnetic field was a dipole inclined by about 10° to the solar rotation axis [*Zhao and Hoeksema*, 1996]. The lack of a significant latitudinal gradient in the radial magnetic field implied that magnetic field was transported to lower latitudes by a nonradial coronal expansion and that heliospheric currents were entirely confined to the heliospheric current sheet (HCS).

[3] The large-scale structure of the expanding solar corona is determined largely by the pattern of magnetic fields on the solar photosphere. A number of studies have attempted to match Ulysses observations by solving the equations of magnetohydrodynamics (MHD) in two and three dimensions with the observed photospheric field taken as the boundary condition. Using synoptic maps from Wilcox Solar Observatory and a three-dimensional polytropic model, *Mikić and Linker* [1996] and *Mikić et al.* [1999] computed the position of the HCS for periods in 1993 and 1995 and found it consistent with Ulysses observations. *Stewart and Bravo* [1997] used Ulysses data as input for an axisymmetric model that included collisional heat conduction and assumed a dipolar field at the solar surface. For a prescribed magnetic field geometry, *Sittler and Guhathakurta* [1999] developed a semiempirical model that used Ulysses observations as well as electron density profiles inferred from white light coronograph data. By specifying a latitude-dependent volumetric heating function and the magnetic field at the solar surface as a combination of dipole and octupole terms, *Gombosi et al.* [2000] and *Groth et al.* [2000] were able to solve the three-dimensional MHD to model the solar wind out to 1 AU. Their results were compared with Ulysses observations.

[1]Also at Institute of Physics, University of St. Petersburg, St. Petersburg, Russia.

0148-0227/03/2002JA009777

[4] To produce a fast wind of relatively low density while preserving reasonable agreement with the plasma density observed at the coronal base, an additional source of momentum and/or energy must be incorporated into the models [*Munro and Jackson*, 1977; *Barnes et al.*, 1995]. Without the additional acceleration, density profiles versus heliocentric distance are too "flat," that is the ratio of the density at 1 AU to the coronal density is too high [*Hundhausen*, 1972, p. 54]. Consequently, the coronal density will be too low if the interplanetary density matches observations [*Stewart and Bravo*, 1997], or the interplanetary density will be too high if the coronal density is close to that inferred observationally. One approach to describing the additional momentum and energy is to use parametric functions without specifying a physical mechanism. That was done by *Wang et al.* [1998] and *Suess et al.* [1999], who constructed an axisymmetric model for the region extending to 10 $R_\odot$ (where $R_\odot$ is the solar radius). Another possibility is to incorporate the additional acceleration by applying an ad hoc procedure as in the model of *Riley et al.* [2001], which consists of self-consistent solutions in two regions $r \leq 30\ R_\odot$ and $\geq 30\ R_\odot$. While the inner boundary condition for the outer region is generally determined from the solution in the inner region, the flow speed at the interface between the two solutions is artificially modified to increase exponentially with the distance from the boundary between open and closed magnetic field lines. That good agreement with Ulysses observations obtained by *Riley et al.* [2001] shows once again the necessity for incorporating the additional acceleration into solar wind models.

[5] Among the numerous possible sources of additional acceleration, Alfvén waves is one of the most attractive. The ability of the waves to produce an additional non-thermal acceleration and to bring models into agreement with observations both near the Sun and at large distances was recognized 3 decades ago [*Belcher*, 1971; *Alazraki and Couturier*, 1971]. The idea was exploited extensively in one-dimensional models with flow tube geometries prescribed more or less arbitrarily ab initio [e.g., *Jacques*, 1978; *Hollweg*, 1978; *Esser et al.*, 1986; *Wang*, 1993; see also review *Hollweg and Isenberg*, 2002]. It appears to be very attractive and natural to combine the wave acceleration mechanism with two-dimensional and three-dimensional approaches to solar corona and solar wind MHD modeling in which the flow geometry is determined self-consistently.

[6] The simplest approach for incorporating Alfvén waves into a multidimensional simulation is to use the WKB approximation which statistically describes the effect of the waves on the background flow and vice versa [e.g., *Dewar*, 1970; *Belcher*, 1971; *Jacques*, 1977, 1978; *Hollweg*, 1990]. The WKB approach is appropriate for the waves with wavelengths shorter than local characteristic scales and does not require a high-resolution description of the momentum and energy transformation from the waves to the flow [e.g., *Ofman and Davila*, 1995, 1998; *Ruderman et al.*, 1999; *Grappin et al.*, 2002]. *Roberts* [1989] and *Smith et al.* [1995a] showed that the WKB theory is not in conflict with the observed evolution of intermediate to large-scale interplanetary fluctuations between 0.3 and 20 AU. Both *Roberts* [1989] and *Smith et al.* [1995a] concluded that extrapolating the observed wave flux back to the coronal base under the WKB approximation was insufficient to produce fast solar wind. However, it is possible that coronal waves are damped inside 0.3 AU. Furthermore, coronal observations [e.g., *Hassler et al.*, 1990] indicate the presence of velocity fluctuations that may produce an energy flux larger than that expected from the WKB extrapolation. Thus it does not appear unreasonable to explore the consequences on coronal outflow implied by a flux of Alfvén waves with amplitudes of 30–50 km s^{-1} emanating from the Sun. To have a wave energy flux that matches the observations, it is necessary to include wave damping. The physical damping mechanism is, however, unclear, but it seems reasonable to approximate it using an exponential damping length, as is frequently done to approximate coronal heating. In this paper we avoid dealing with the coronal heating mechanism [see, e.g., *Lionello et al.*, 2001] by placing the inner boundary somewhere just outside the transition region, i.e., at the so-called "coronal base."

[7] This approach of using the wave ponderomotive force as an additional source of solar wind acceleration is often called a "wave-driven" model. It is sometimes dismissed because it is thought to not provide sufficient acceleration to fit the outflow speeds inferred from interplanetary scintillation measurements and from the coronal electron density profiles and particle flux observations at 1 AU [see *Grall et al.*, 1996; *Guhathakurta and Fisher*, 1998; *Guhathakurta et al.*, 1999]. The speeds reported by *Grall et al.* [1996] were however speeds of the density fluctuations rather than the actual flow velocities. Close to the Sun, where the propagation speeds of fast and Alfvén waves are much higher than the flow speed, the inference of Grall et al. that the wind acceleration is virtually completed by 10 $R_\odot$ does not seem to be conclusive. The velocity profiles in the works of *Guhathakurta and Fisher* [1998] and *Guhathakurta et al.* [1999] appear to support the results of *Grall et al.* [1996] but do not show speeds exceeding values of $\sim$600 km s^{-1} below 10 $R_\odot$. It is not implausible that such speeds could be obtained using wave-driven models.

[8] *Usmanov et al.* [2000] (hereafter referred to as Paper 1) developed such an axisymmetric model in which a steady coronal outflow was simulated in a dipolar magnetic field. In that work the WKB Alfvén waves were explicitly invoked as a means of heating and accelerating the solar wind and a reasonable steady-state two-dimensional solution was obtained. The dipole field strength and the amplitude of Alfvén waves at 1 $R_\odot$ were chosen to obtain a good fit to Ulysses data. A self-consistent solution was constructed by applying a time relaxation technique in the region near the Sun. In the outer computational region, a marching-along-radius numerical algorithm was used. The solution formed a bimodal structure of fast and slow wind, as observed, and the computed parameters were generally consistent with Ulysses data and with typical parameters at the coronal base.

[9] Although the bimodality is already present in the models without waves [e.g., *Pneuman and Kopp*, 1971; *Steinolfson et al.*, 1982, also compare Paper 1], faster and more tenuous wind from polar regions and slower and denser wind above the streamer in the heliospheric plasma sheet, the contrast is too small and does not match the pronounced latitudinal variation observed by Ulysses (Paper 1). The addition of waves increases the velocity of

the faster wind and lowers its density to observed values but has only a relatively small effect on the slower wind belt, where the divergence of flow tubes is much higher, plasma is denser, and the plasma beta is significantly above unity.

[10] The two-dimensional study of Paper 1 neglected all gradients in the azimuthal direction and the north-south symmetry was enforced by assuming the solar magnetic field to be a dipole perpendicular to the solar equatorial plane. The dipole assumption led to a heliospheric current sheet that was aligned with the equatorial plane, while the actual HCS deviated slightly from that plane [*Smith et al.*, 1995b]. To account for that effect the model curves in Paper 1 were shifted artificially by 15° north and south, emulating a relatively wide belt of slow wind near the solar equator. In the present study we relax the assumptions of axial and north-south symmetry so that we can model the HCS warping more consistently. The basic idea is to use essentially the same solution for the inner region as in Paper 1 but to transform it to match the observed orientation of the solar dipole, and than extend that tilted-dipole solution to the Earth's orbit through the outer region using a three-dimensional model. By taking into account the solar rotation in the outer region, we are able to incorporate the interaction between faster and slower solar wind streams and the azimuthal component of magnetic field.

2. Model Formulation

[11] The governing MHD equations for a single-fluid polytropic flow driven by thermal and Alfvén wave pressure gradients, including solar rotation are

$$\frac{\partial \rho}{\partial t} + \nabla \cdot \rho \mathbf{v} = 0, \tag{1}$$

$$\frac{\partial (\rho \mathbf{v})}{\partial t} + \nabla \cdot \left[\rho \mathbf{v}\mathbf{v} + \left(P + \frac{\mathcal{E}}{2} + \frac{B^2}{8\pi} \right) \mathbf{I} - \frac{\mathbf{B}\mathbf{B}}{4\pi} \right] + \rho \left[\frac{GM_\odot}{r^2} \hat{r} + 2\boldsymbol{\Omega} \times \mathbf{v} + \boldsymbol{\Omega} \times (\boldsymbol{\Omega} \times \mathbf{r}) \right] = 0, \tag{2}$$

$$\frac{\partial \mathbf{B}}{\partial t} = \nabla \times (\mathbf{v} \times \mathbf{B}), \tag{3}$$

$$\frac{\partial}{\partial t} \left[\frac{\rho}{2} \left(v^2 - |\boldsymbol{\Omega} \times \mathbf{r}|^2 \right) + \frac{P}{\gamma - 1} + \frac{B^2}{8\pi} - \frac{\rho GM_\odot}{r} + \mathcal{E} \right] + \nabla \cdot \left\{ \left[\frac{\rho}{2} \left(v^2 - |\boldsymbol{\Omega} \times \mathbf{r}|^2 \right) + \frac{\gamma P}{\gamma - 1} - \frac{\rho GM_\odot}{r} \right] \mathbf{v} + \frac{\mathbf{B}}{4\pi} \times (\mathbf{v} \times \mathbf{B}) + \left(\frac{3}{2} \mathbf{v} + \mathbf{V}_A \right) \mathcal{E} \right\} = 0, \tag{4}$$

$$\frac{\partial \mathcal{E}}{\partial t} + \nabla \cdot [(\mathbf{v} + \mathbf{V}_A)\mathcal{E}] = -\frac{\mathcal{E}}{2} \nabla \cdot \mathbf{v} - |\mathbf{v} + \mathbf{V}_A| \frac{\mathcal{E}}{L}, \tag{5}$$

where the dependent variables ρ, $\mathbf{v}$, $\mathbf{B}$, P, and $\mathcal{E}$ are the plasma density, the flow velocity in the frame rotating with the Sun, the magnetic field, the thermal pressure, and the Alfvén wave energy density, respectively. $M_\odot$ is the solar mass, $\boldsymbol{\Omega}$ is the solar angular velocity vector, γ is the polytropic index, t is the time, r is the heliocentric distance, G the gravitational constant, $\hat{r}$ is a unit vector in the radial direction, and $\mathbf{I}$ is the unit matrix. $\mathbf{V}_A$ is the velocity of outward propagating Alfvén waves defined such that $\mathbf{V}_A = \mathbf{B}/(4\pi\rho)^{1/2}$ if $B_r \geq 0$ and $\mathbf{V}_A = -\mathbf{B}/(4\pi\rho)^{1/2}$ if $B_r < 0$. The Alfvén wave effects are incorporated into the governing equations in the WKB limit and it is assumed that the waves are damped by a mechanism that may be characterized by a dissipation length L.

[12] As in previous work [*Usmanov*, 1993a, 1993b; *Usmanov and Dryer*, 1995; Paper 1], we divide the computational domain into two regions: an outer region where the flow will be both supersonic and super-Alfvénic; and an inner region (I) (1–20 $R_\odot$), where the equations (1)–(5) are solved by the time-relaxation method, i.e., the governing equations are integrated in time up to a steady state. In the outer region (II) (20 $R_\odot$ – 10 AU) the solution is constructed by forward integration along the hyperbolic radial coordinate [*Pizzo*, 1982, 1991]. The computations in region I are performed on a grid of 304 × 94 with the angular spacing of 1° and with the radial step increasing linearly from 0.01 $R_\odot$ at 1 $R_\odot$ to ~0.2 $R_\odot$ at 20 $R_\odot$. The angular resolution for integration in radial direction in region II is 1° in latitude and 2° in longitude. We note here that we performed also a number of runs with different resolutions both along radius (with up to 454 radial points) and latitude and obtained the results which are very close to those presented in the next section.

[13] The initial and boundary conditions are similar to those in Paper 1. The driven Alfvén wave velocity amplitude $\delta V = (\mathcal{E}/\rho)^{1/2}$ at the poles at 1 $R_\odot$ is assumed to be 35 km s^{-1}, close the upper limit value inferred by *Hassler et al.* [1990]. The wave velocity amplitude then decreases as $\cos^{1/2}\theta$ towards the equator. The strength of the surface dipole field on the poles was chosen to be 14 G. The plasma temperature and density in the initial state at 1 $R_\odot$ are 1.8×10^6 K and 5×10^7 particles cm^{-3}, respectively, and the dissipation length for Alfvén waves is L = 80 $R_\odot$. The polytropic index is taken to be different from the adiabatic value to account implicitly for thermal conduction: γ = 1.12 in region I, and γ = 1.46 [*Totten et al.*, 1995] in region II. Note that the values above were selected to optimize the fit to Ulysses data.

[14] To solve the relaxation problem in region I, we apply a TVD (Total Variation Diminishing) Lax-Friedrichs algorithm with the Woodward limiter [*Tóth and Odstrčil*, 1996]. The field-interpolated central difference approach suggested by *Tóth* [2000] is used to maintain the $\nabla \cdot \mathbf{B} = 0$ constraint. The code is written to run on massively parallel computers using the Message Passing Interface. The relaxation procedure is somewhat time consuming; a typical run takes about 2.5 hours using 32 processors on the Origin 3000 system at the NASA Ames Research Center. The integration along the radius in region II is performed with the numerical scheme of *MacCormack* [1971] and requires incomparably fewer computational resources. It takes only about 800 radial steps and several minutes of computational time on a PC computer.

3. Simulation Results

[15] We start from an initial state with radial flow in a dipolar magnetic field and integrate the region I equations

in time until a steady state is achieved. Once the axisymmetric solution is obtained, it is transformed into a three-dimensional distribution that matches approximately the orientation of the solar dipole during the first fast latitude scan of Ulysses (September 1994–July 1995). We compute the dipole orientation from the expansion coefficients for the photospheric field inferred at the Wilcox Solar Observatory (WSO) from the line-of-sight boundary condition and the source surface at 2.5 $R_\odot$. We ignore the fact that orientation of the solar dipole changed slightly during the Ulysses transition and use the dipole parameters inferred from solar rotation 1887 (at the beginning of the transition, September–October 1994). During that time period, the dipole axis was 9.7° from the rotation axis at an azimuth (in the Northern Hemisphere) of 330°.

[16] The boundary between regions I and II was placed in the supersonic and super-Alfvénic flow regime, ensuring that the solution in region II depends only on the flow parameters on the boundary. The transformed solution at the upper radial level of region I is used to initialize integration of the equations along radius through region II out to 10 AU.

3.1. Meridional Structure From 1 $R_\odot$ to 10 AU

[17] Figure 1 shows contour plots of the computed flow and magnetic field parameters in the meridional plane ϕ = 0, which was chosen arbitrarily to demonstrate a cut through the entire solution from 1 $R_\odot$ to 10 AU. Because the radial scale is logarithmic, the near-Sun region is emphasized and the region outside 1 AU occupies only the periphery of each plot. The velocity pattern in Figure 1a includes a stagnation region near the equator (approximately inside the innermost level of 5 km s^{-1}) where the magnetic tension is sufficient to suppress plasma outflow. The figure also shows two polar coronal holes at latitudes north of ~60° where plasma is flowing outward, filling the entire heliosphere. It is clear that the radial velocity distribution is bimodal and except for a slower wind band around the equator depends only slightly on latitude. The magnetic field magnitude (Figure 1b) which varies as $(3\cos^2\theta + 1)^{1/2}$ on the solar surface (from 14 G on the poles to 7 G on the equator) also converges to an almost latitudinally independent distribution at distances $\gtrsim$20 $R_\odot$. This redistribution is associated with the meridional flows (Figure 1c) caused by the meridional magnetic pressure gradient forcing the plasma to flow towards the equator (the peak meridional velocity in our case is ~140 km s^{-1}). In its turn, the meridional flows relieve the meridional gradient in the magnetic pressure and produce a latitudinally uniform structure by the distance where the flow becomes radial. This effect was first described by *Suess et al.* [1977] and then studied in more detail by *Suess and Smith* [1996], *Bravo and Stewart* [1996], and *Suess et al.* [1999] (also see Paper 1). This feature of the solutions accounts for the lack of a significant magnetic pressure gradient in the Ulysses observations.

[18] The meridional flows not only relax the imposed magnetic field gradients, but they also redistribute mass flux in latitude by pulling the material around the stagnation region down to lower latitudes. The meridional flows create a belt of higher density that can be associated with the heliospheric plasma sheet [*Winterhalter et al.*, 1994]. The contours of number density shown in Figure 1d also show latitudinally independent profiles with the exception of the plasma sheet where the density is increased and the flow is relatively slow. As was shown in Paper 1, the latitudinal redistribution due to the equatorward meridional flows is essentially completed (i.e., the flow becomes radial) at the distance where the modified plasma beta parameter $\beta_T = 8\pi(P + \mathcal{E})B^2 = 1$. Further from the Sun, at distances $r \geq 20$–30 $R_\odot$ where the magnetic field is not anymore dominant and $\beta_T > 1$, a second redistribution, this time with meridional flows directed poleward, takes place which somewhat relaxes the equatorward gradient of plasma pressure in the plasma sheet. The poleward flows in the region $\beta_T > 1$ are relatively small and only slightly redistribute the magnetic field in latitude.

[19] In the initial state, the amplitude of Alfvén waves δV varies as $\cos^{1/2}\theta$ so that the wave amplitudes are maximum at the poles of the dipole and 0 on the equator. During the relaxation process, that initial δV evolves together with the plasma and magnetic field parameters. The resulting state (after extending the solution through region II to 10 AU) is shown in Figure 1e. As discussed in Paper 1, during relaxation we impose the condition $\mathcal{E} = 0$ inside the streamer so that δV is virtually zero in the stagnation region and remains close to zero in a region near the equator where wave acceleration is therefore negligible. Outside that region, δV is only slightly dependent on latitude. A similar lack of dependence on latitude in fast wind of the plasma temperature is seen in Figure 1f. However, note that a relatively hot streamer-like structure covers the stagnation region and extends out to ~20 $R_\odot$. In that structure, the temperature is higher near the equator and decreases with latitude. At larger distances, the temperature in the slow wind increases with latitude until one reaches the fast flow regime.

[20] As expected, in region II the tilted, rotating dipolar solar magnetic field causes fast and slow wind streams to interact, producing a warp in the plasma sheet that becomes more pronounced with the heliocentric distance. The effect is most evident in the radial and meridional velocity plots.

[21] Figure 2 shows variations of velocity and density with latitude in the plane ϕ = 0 for various heliocentric distances from 1 $R_\odot$ to 1 AU (~215 $R_\odot$). The figure demonstrates again the bimodal structure of the heliosphere, with slower wind near the equator and uniform fast wind at higher latitudes. The minimum flow speed at 1 AU is less than 400 km s^{-1} near the heliospheric equator. The flow speed then climbs rapidly with latitude, reaching ~700 km s^{-1} by ~15°, and then increases slowly towards the pole. At 1 AU, the number density is ~2.5 cm^{-3} in the fast wind and climbs to ~25 cm^{-3} near the equator. In the ϕ = 0 meridional plane, the stream interaction causes the latitudinal velocity gradient in the Northern Hemisphere to be steeper than it is in the Southern Hemisphere. The profiles are inverted on the opposite side of the Sun so that at ϕ = 180° the velocity gradient is steeper in the Southern Hemisphere.

[22] The simulation shows that the velocity of slow wind reaches a sharp minimum near the heliospheric equator (Figure 3). In Figure 3 the simulation is compared directly with solar wind speeds observed by Helios 1 and 2 and IMP-8 as a function of angular distance from the helio-

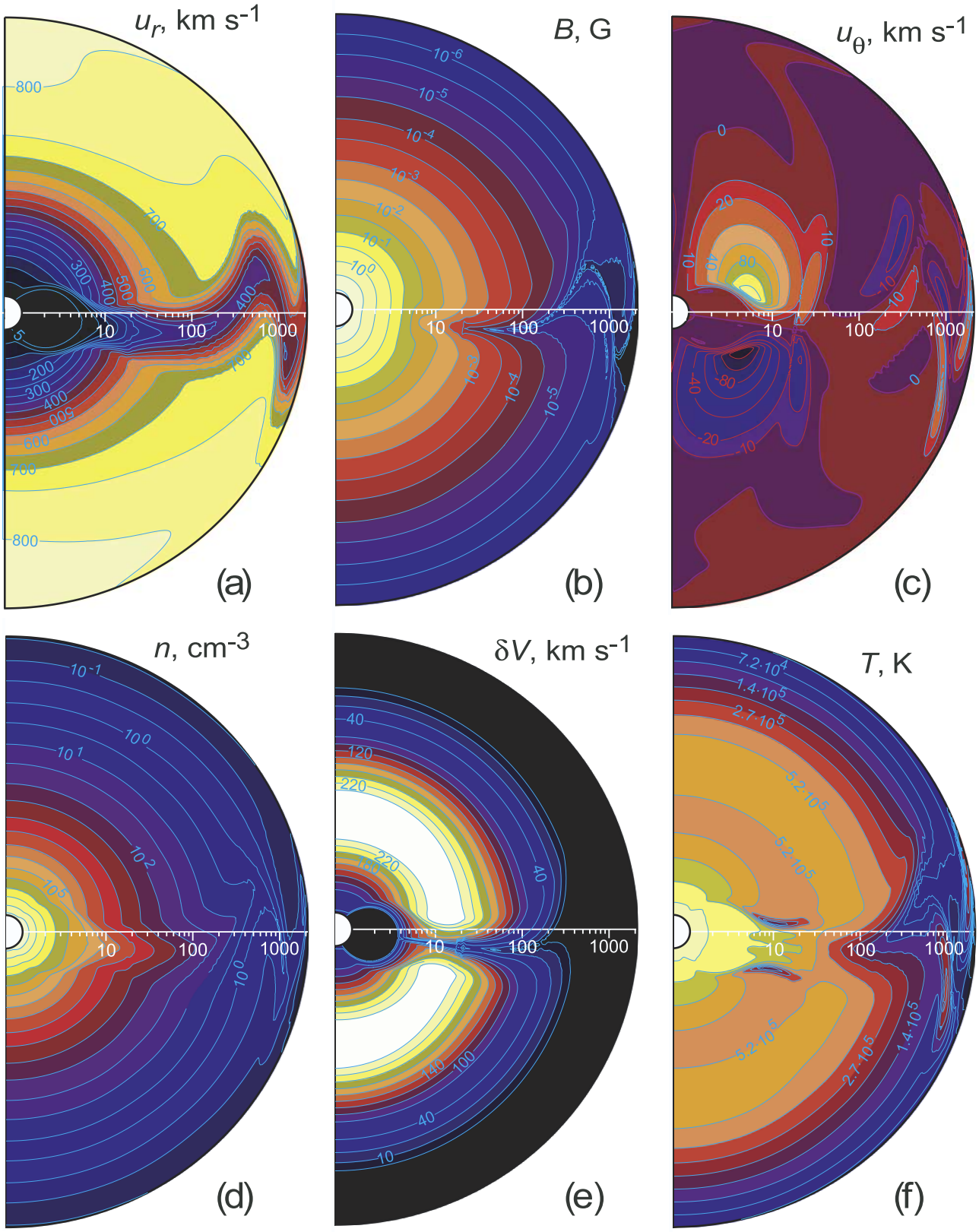

Figure 1. Contour plots of (a) the radial velocity in km s^{-1}, (b) magnetic field strength in Gauss, (c) meridional velocity in km s^{-1}, (d) number density in particles cm^{-3}, (e) amplitude of Alfvén waves in km s^{-1}, and (f) plasma temperature in Kelvin in the meridional plane at $\phi = 0$. The radial range is from 1 $R_\odot$ to 10 AU.

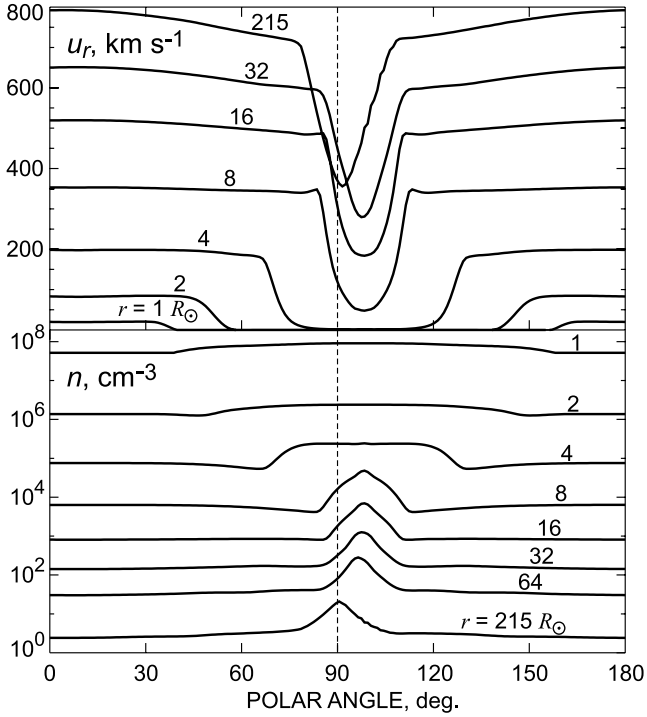

Figure 2. The radial velocity u_r and the number density n versus polar angle at the indicated radial distances in the meridional plane $\phi = 0$.

spheric current sheet [*Bruno et al.*, 1986]. In constructing the comparison, we chose the meridional planes for which the minimum velocities coincided with the equator. To project the data from the three spacecraft back to the Sun, *Bruno et al.* [1986] used a constant-velocity approximation. In the figure, we show a single model profile from 0.3 AU (near the perigee of the Helios spacecraft) and two others from 1 AU. Because the 1 AU profiles are markedly asymmetric about equator, we chose the pair to be at the antipodal longitudes. However, the stream interaction had

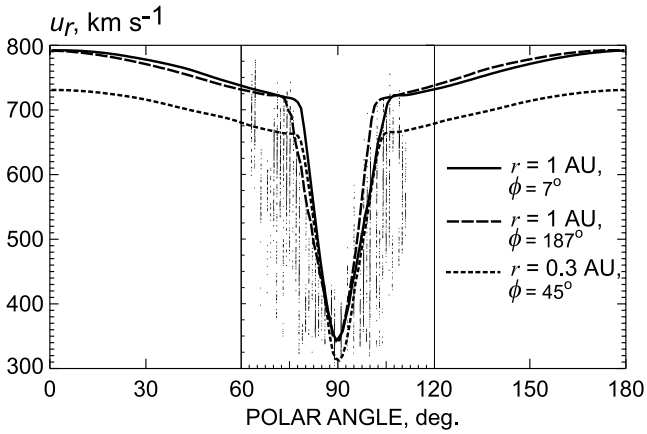

Figure 3. Latitudinal profiles from the model at 0.3 and 1 AU and solar wind speeds observed by Helios 1 and 2 and IMP-8 versus angular distance from the heliospheric current sheet from *Bruno et al.* [1986].

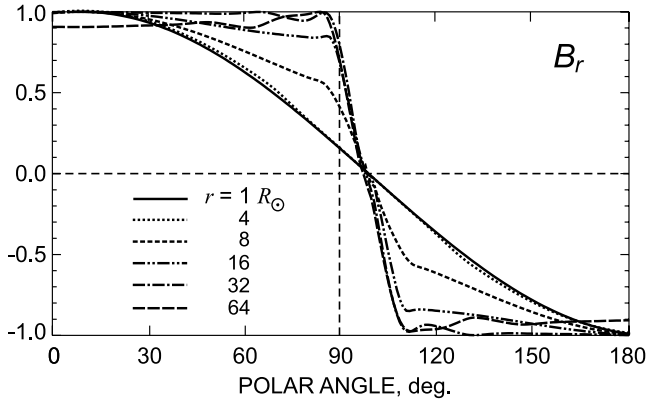

Figure 4. Variations of the radial magnetic field B_r versus polar angle at radial distances 1–64 $R_\odot$ (normalized to the maximum value in the Northern Hemisphere).

not produced a noticeable asymmetry at 0.3 AU, so only a single profile is shown. Although the latitudinal width of the model curves is generally narrower than is the data, the general behavior is similar. Note that the simulation was constructed to fit the observations taken between 1994 and 1995 while the data used by *Bruno et al.* [1986] were from 1976–1977.

[23] The evolution of the radial magnetic field with heliocentric distance is shown in Figure 4. Note that B_r becomes increasingly independent of latitude as heliocentric distance increases to 32 $R_\odot$. This redistribution is driven by the equatorward flows relieving the gradient imposed at 1 $R_\odot$. At larger distances, the poleward flows redistribute B_r maintaining the small equatorward gradient outside the plasma sheet [cf., Paper 1]. This result appears to be in agreement with the Ulysses observations of *Smith et al.* [2000], who found an increase in $|B_r|$ with latitude at mid-latitudes and the absence of a gradient at high latitudes.

3.2. Plasma and Magnetic Field at 1 $R_\odot$ and 1 AU

[24] Contour maps of the flow parameters in the heliographic coordinates are shown in Figure 5. The left three panels display the radial magnetic field B_r, radial velocity u_r, and number density n at the coronal base (1 $R_\odot$). The B_r distribution at 1 $R_\odot$ is dipolar and is set as a boundary condition during the relaxation process. The contour of u_r at 1 $R_\odot$ (black indicates the region without outflow, i.e., $u_r = 0$) provides a view of solar wind sources at the coronal base. The wind is streaming out of the polar regions extending down by $\sim$30° from the dipole axis. This is consistent with observations of coronal holes at the time of Ulysses traversal [*Gosling et al.*, 1995]. In these outflow regions (the "coronal holes" of the simulation) the outflow speed is $\sim$20 km s^{-1} (see also Figure 2), while $n \sim 5 \times 10^7$ cm^{-3}, which is markedly lower than in the stagnation belt nearby where n sharply increases to $\sim 9 \times 10^7$ cm^{-3}. The distribution of plasma temperature (not shown) is similar to that of density; the temperature changes from 1.8×10^6 K in polar regions to 1.9×10^6 K near the equator.

[25] At 1 AU (the right-hand panels in Figure 5), the model wind is distinctly bimodal. There are no prominent

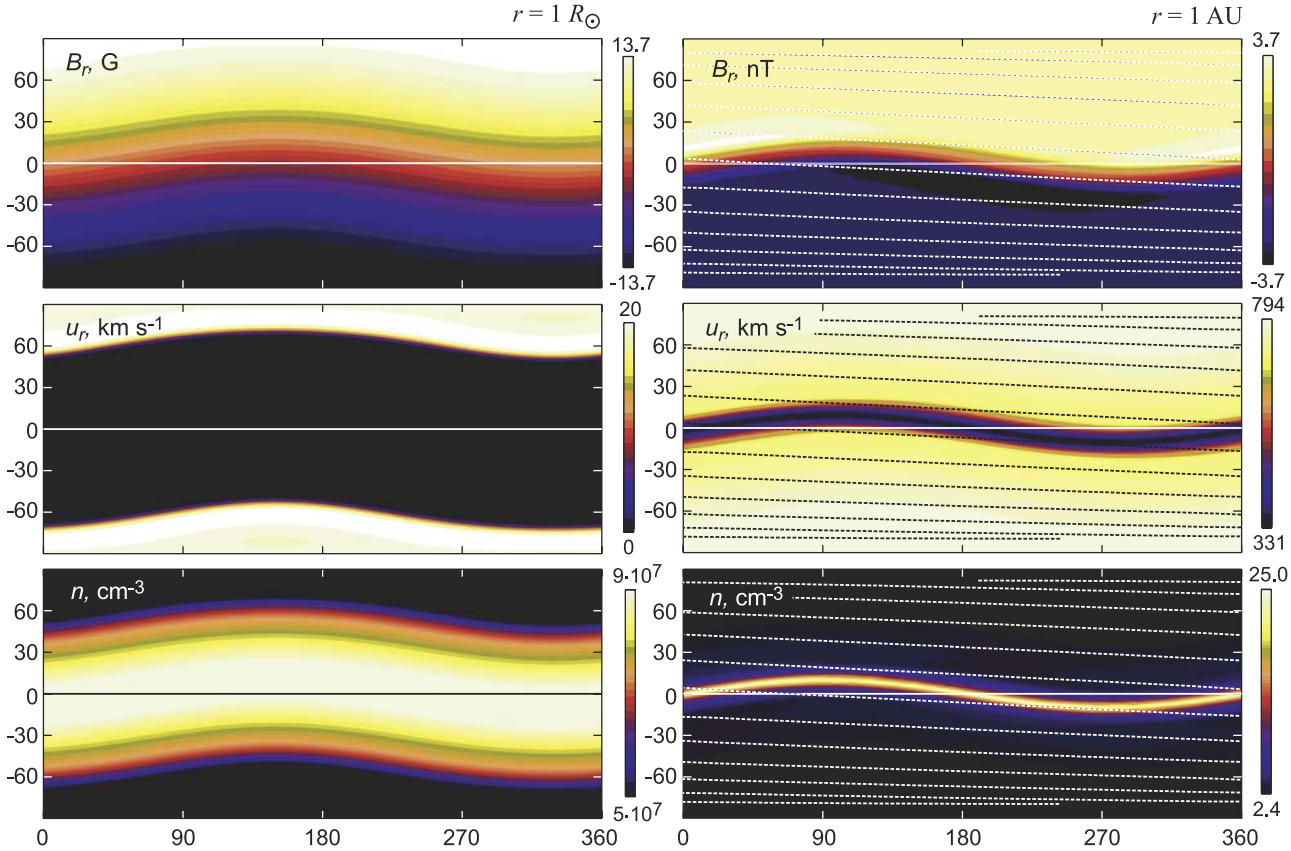

Figure 5. Contour plots of the radial magnetic field, the radial velocity and the number density in the heliographic coordinates at 1 $R_\odot$ (left panels) and at 1 AU (right panels). Ulysses' trajectory is shown on the right panels by dotted lines. The stagnation region (of no mass outflow) is filled with black on the left middle plot.

variations in either plasma or magnetic field except for a narrow equatorial belt where the flow is relatively dense and slow and where B_r changes sign. The trajectory of Ulysses in the heliographic coordinates during solar rotations 1887–1898 is superimposed on the plots and consists of slightly inclined lines depicting its travel from south to north polar regions.

3.3. Further Comparison With Ulysses Observations

[26] A direct comparison of Ulysses observations with the model results is presented in Figure 6. The daily averages of Ulysses data were scaled to 1 AU assuming that B_r and n to fall off with radial distance as r^{-2}, the azimuthal magnetic field B_ϕ as r^{-1}, and the temperature T as $r^{-2(\gamma-1)}$ with $\gamma = 1.46$. Inclining the solar dipole with respect to the solar rotation axis is seen to produce fairly good agreement between the model and the Ulysses observations, including the latitudinal extension of the slower wind belt. Note that the normalization of Ulysses data to 1 AU is not required for this comparison since the computational region extends to 10 AU. However, the normalization used eliminates relatively easy-to-follow radial variations and emphasizes latitudinal structure. The computed temperature is somewhat higher than that observed, but that could be adjusted by varying the damping length L; larger L would provide less wave dissipation and ultimately lower temperatures. The electron temperature at large heliocentric distances is, however, larger than the proton temperature so that the (higher) single fluid temperature obtained in the simulation is not necessarily in conflict with the proton temperature observed by Ulysses.

3.4. Comparison With Coronal Density Models

[27] As discussed above, the simulated density correlates reasonably well with Ulysses observations. On the other end, one can also compare the simulation with empirical models of coronal electron density. There are a number of such models that relate to solar minimum. Figure 7 shows a superposition of our results for the pole and the equator with the models of *Allen* [1973], *Saito et al.* [1970], *Munro and Jackson* [1977], and *Guhathakurta et al.* [1999]. (Allen's and Saito et al.'s distributions were computed from the analytical approximations given by *Osherovich et al.* [1984].)

[28] In general, the empirical models and the simulation agree close to 1 $R_\odot$, at larger distances the simulated densities are systematically higher. The peak difference in polar values is close to a factor of 4 at 3–4 $R_\odot$. The equatorial density matches almost perfectly the *Allen* [1973] and *Saito et al.* [1970] empirical curves up to 3 $R_\odot$ but again is higher at larger distances. Although the differences appear to be significant, it is well known that there remain uncertainties in the empirical models due to

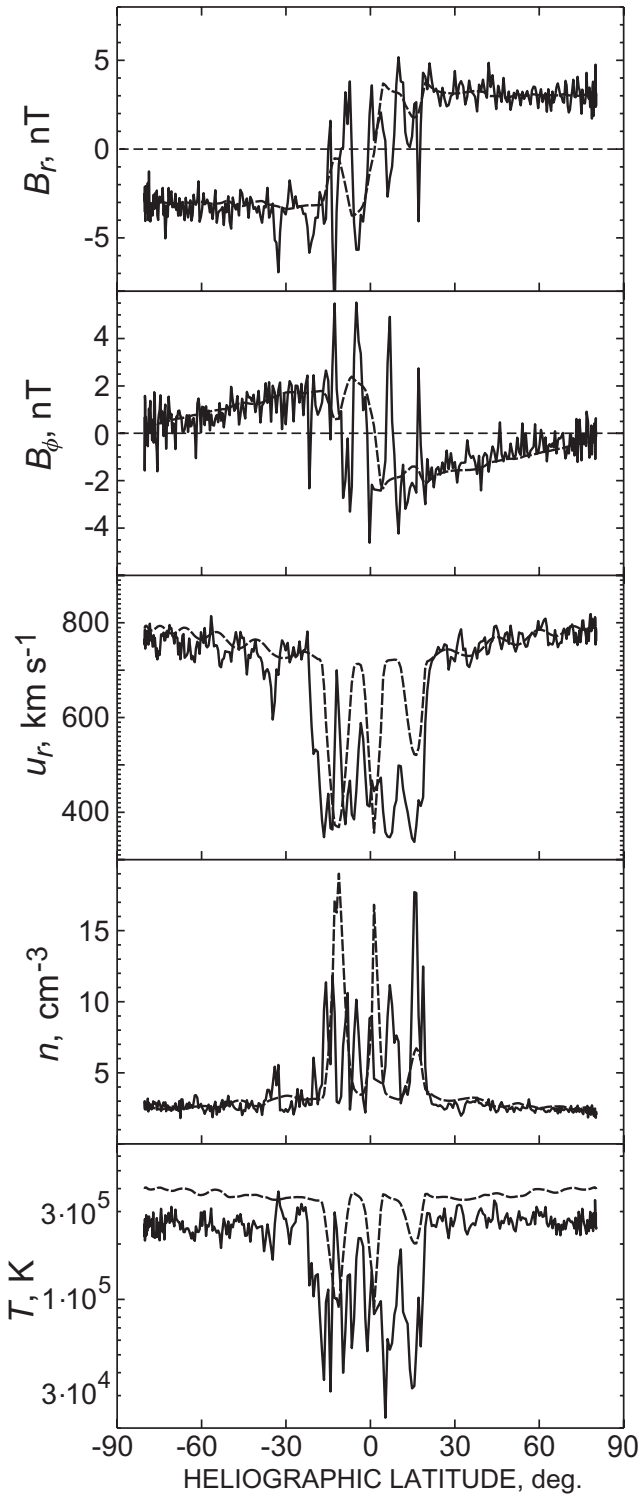

Figure 6. The model output (dashed lines) versus Ulysses data collected during its first fast latitude scan in 1994–1995 (solid lines). The Ulysses data are normalized to conditions at 1 AU.

uncertainties in the modeling procedures and, perhaps more importantly, uncertainties in the calibrations of the observing instruments. Furthermore, there are additional uncertainties in the measurements of polarization brightness. Future work, however, may require modification of our model to lower the coronal density beyond a few $R_\odot$.

3.5. Expansion Factor and Comparison With the Wang-Sheeley Model

[29] The Wang-Sheeley model [*Wang and Sheeley*, 1990] is an empirical relation between the areal expansion factor and the solar wind speed. The expansion factor f_s is defined as the ratio of the solid angles subtended by a magnetic flux tube at a heliocentric distance r and at the coronal base (1 $R_\odot$), i.e., $f_s(r) = (R_\odot/r)^2[B(R_\odot)/B(r)]$, where $B(R_\odot)$ and $B(r)$ are the magnetic field strengths at 1 $R_\odot$ and at the distance r, respectively. It was first found by *Levine et al.* [1977] that the open field regions with a relatively small areal expansion are associated with high-speed streams. Using synoptic maps of photospheric magnetic field from WSO and a potential field source surface model, Wang and Sheeley also obtained an inverse correlation and established an empirical relation between the solar wind speeds observed at the Earth and the expansion factor of flux tubes between the photosphere and the "source surface" at 2.5 $R_\odot$.

[30] In one-dimensional models the expansion factor f_s is usually a free input function. With our model, this function follows from the initial and boundary conditions. Meridional profiles of f_s were discussed in Paper 1; here we present f_s as a function of r. Figure 8a shows the variation of f_s with

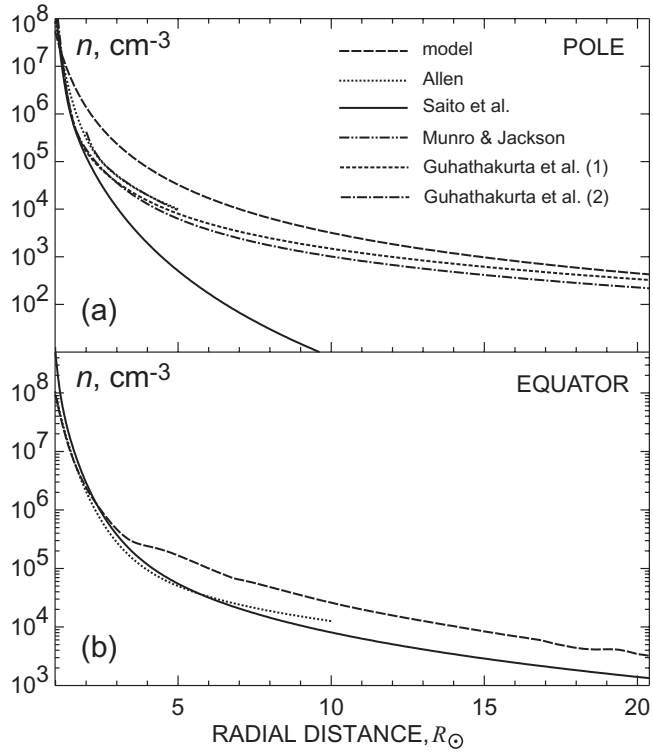

Figure 7. Number density as a function of radius from the present model and from a number of empirical models: (a) the polar hole region and (b) the equatorial region. *Guhathakurta et al.* [1999] provide two analytical approximations for the polar hole inferred from (1) SOHO white-light coronograph measurements and (2) from Spartan 201-03 coronograph data.

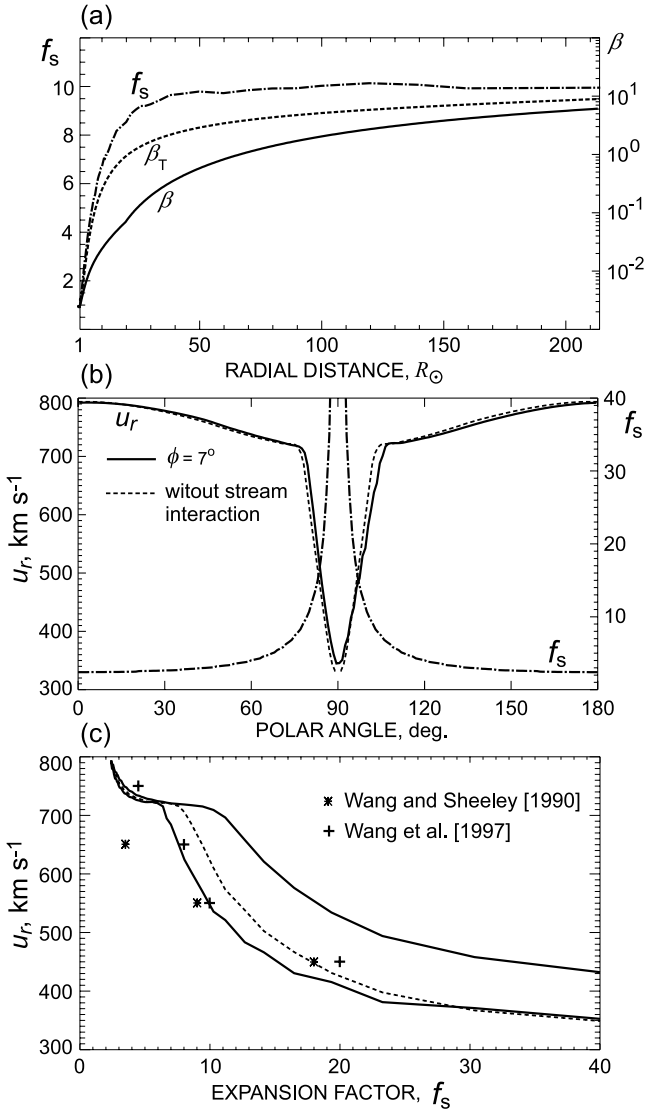

Figure 8. (a) Radial variations of the areal expansion factor f_s, the plasma parameter $\beta = 8\pi P/B^2$ and the modified parameter $\beta_T = 8\pi(P + E)/B^2$. (b) Meridional variations of f_s between 1 and 2.5 $R_\odot$ (dot-dashed line) and the radial velocity u_r at 1 AU. The two curves for u_r are that in the plane $\phi = 7°$ (solid line) and that computed without account for solar rotation (dashed line). (b) u_r versus f_s for the same two meridional profiles of u_r. Stars and crosses indicate the empirical relationships determined by *Wang and Sheeley* [1990] and *Wang et al.* [1997], respectively.

distance along the pole line showing that f_s increases from unity at 1 $R_\odot$ to ~10 at 1 AU, with a largest increase below ~20 $R_\odot$. Also shown are β and the parameter β_T in which P is replaced by the sum of P and E. We showed in Paper 1 and find again in Figure 8a that the dipole field becomes uniform in the region $\beta_T \lesssim 1$, i.e., at $r \lesssim 20$ $R_\odot$ where magnetic forces are relatively important.

[31] From the simulation, one can compute directly both f_s and the velocity at 1 AU and thus compare with the empirical relation deduced by *Wang and Sheeley* [1990]. Figure 8b presents the meridional profiles of u_r at 1 AU and f_s between 1 and 2.5 $R_\odot$, showing clearly that solar wind speed anticorrelates with f_s. f_s increases slowly toward the equator in the fast wind and peaks sharply in the lower speed belt. There are two velocity profiles in this plot: one is that at $\phi = 7°$; the other is calculated without including solar rotation in region II and hence is symmetric about the equator. The superposition of the two velocity profiles emphasizes the effects of solar rotation.

[32] The variations of f_s and u_r with the polar angle can be easily converted into a dependence of u_r on f_s which can be contrasted to the results of *Wang and Sheeley* [1990]. Figure 8c shows the variations for the two velocity profiles shown in Figure 8b. The velocity in the plane $\phi = 7°$ is asymmetric about the equator and its profile has two branches (solid lines). The stars on the panel are the empirical points from *Wang and Sheeley* [1990] and the crosses from an updated version of their model [*Wang et al.*, 1997]. Again, the inverse correlation between u_r and f_s is clearly visible. As one can see, the simulation results are in good agreement with the updated empirical model of Wang and Sheeley.

4. Conclusions

[33] We have developed a global MHD model of the solar corona and solar wind designed to reproduce Ulysses observations during its first fast latitude transition in 1994–1995. The model includes Alfvén wave momentum and energy addition into open field regions that provides an additional acceleration for the solar wind flow. The simulation domain extends from the coronal base to 10 AU and consists of two regions with a boundary between them placed at 20 $R_\odot$ ensuring that in Region II the flow is both supersonic and super-Alfvénic. The inner region steady-state solution is obtained by the time relaxation method. The solution in the outer region depends only on the values at the interregion boundary and is constructed by forward integration along radius. The original axisymmetric model of Paper 1 is modified to include an inclined dipole and three-dimensional computations in the region outside 20 $R_\odot$. Also, the solar rotation is incorporated into the present model and therefore the stream interactions are treated self-consistently.

[34] We have shown that the simulated variations of plasma and magnetic field parameters and in particular the extension of slow wind belt agree fairly well with the Ulysses observations. In the present tilted-dipole model, this extension results from the latitudinal oscillations of a relatively narrow region of slower velocities due to warping of the heliospheric plasma/current sheet and the solar rotation. While the fast wind characteristics are reproduced reasonably well, the model variations in the slower wind bear much less resemblance to observations. We believe that the latter can be attributed at least in part to the dipole approximation for the solar magnetic field. To reproduce the slower wind observations in more detail, we are implementing a fully three-dimensional model that will incorporate higher harmonic model of the solar magnetic field.

[35] We have compared also the outcome from our simulation with the results of *Bruno et al.* [1986] on the solar wind speed dependence of latitude, with the empirical distributions of electron density in solar corona, and with

the Wang-Sheeley empirical model [*Wang and Sheeley*, 1990] that relates the areal expansion factor to the solar wind speed. On the whole, these comparisons appear to support our model, with the exception that within $\sim 20\ R_\odot$ the simulated coronal density is somewhat higher than those inferred from polarization brightness measurements.

[36] **Acknowledgments.** This work was performed while one of the authors (AVU) held a National Research Council Senior Research Associateship at the NASA Goddard Space Flight Center. Ulysses plasma and magnetic field data were obtained from the NSSDC COHOWeb. Wilcox Solar Observatory data were obtained from http://quake.stanford.edu/~wso, courtesy of J. T. Hoeksema. We thank Xue Pu Zhao for bringing the updated version of the Wang-Sheeley model to our attention. We would like to acknowledge the support of James Fisher, Manager for High Performance Computing at the Goddard Space Flight Center, for helping to arrange use of computing resources at the NASA Advanced Supercomputing Division.

[37] Shadia Rifai Habbal thanks Roberto Lionello and another referee for their assistance in evaluating this paper.

References

Alazraki, G., and P. Couturier, Solar wind acceleration caused by the gradient of Alfvén wave pressure, *Astron. Astrophys.*, *13*, 380–389, 1971.

Allen, C. W., *Astrophysical Quantities*, 3rd ed., Atholone Press, London, 1973.

Balogh, A., E. J. Smith, B. T. Tsurutani, D. J. Southwood, R. J. Forsyth, and T. S. Horbury, The heliospheric magnetic field over the south polar region of the Sun, *Science*, *268*, 1007–1010, 1995.

Barnes, A., P. R. Gazis, and J. L. Phillips, Constraints on solar wind acceleration mechanisms from Ulysses plasma observations: The first polar pass, *Geophys. Res. Lett.*, *22*(23), 3309–3311, 1995.

Belcher, J. W., Alfvénic wave pressures and the solar wind, *Astrophys. J.*, *168*, 509–524, 1971.

Bravo, S., and G. A. Stewart, Latitudinal variation of the heliospheric magnetic field during solar minimum, *Geophys. Res. Lett.*, *23*(22), 3271–3274, 1996.

Bruno, R., U. Villante, B. Bavassano, R. Schwenn, and F. Mariani, In-situ observations of the latitudinal gradients of the solar wind parameters during 1976 and 1977, *Solar Phys.*, *104*, 431–445, 1986.

Dewar, R. L., Interaction between hydromagnetic waves and a time-dependent, inhomogeneous medium, *Phys. Fluids*, *13*(11), 2710–2720, 1970.

Esser, R., E. Leer, S. R. Habbal, and G. L. Withbroe, A two-fluid solar wind model with Alfvén waves: Parameter study and application to observations, *J. Geophys. Res.*, *91*(A3), 2950–2960, 1986.

Forsyth, R. J., A. Balogh, T. S. Horbury, G. Erdös, E. J. Smith, and M. E. Burton, The heliospheric magnetic field at solar minimum: Ulysses observations from pole to pole, *Astron. Astrophys.*, *316*, 287–295, 1996.

Gombosi, T. I., D. L. De Zeeuw, C. P. T. Groth, K. G. Powell, and Q. F. Stout, Multiscale MHD simulation of a coronal mass ejection and its interaction with the magnetosphere-ionosphere system, *J. Atmos. Sol. Terr. Phys.*, *62*(16), 1515–1525, 2000.

Gosling, J. T., S. J. Bame, W. C. Feldman, D. J. McComas, J. L. Phillips, B. Goldstein, M. Neugebauer, J. Burkepile, A. J. Hundhausen, and L. Acton, The band of solar wind variability at low heliographic latitudes near solar activity minimum: Plasma results from the Ulysses rapid latitude scan, *Geophys. Res. Lett.*, *22*(23), 3329–3332, 1995.

Grall, R. R., W. A. Coles, M. T. Klinglesmith, A. R. Breen, P. J. S. Williams, J. Markkanen, and R. Esser, Rapid acceleration of the polar solar wind, *Nature*, *379*, 429–432, 1996.

Grappin, R., J. Léorat, and S. R. Habbal, Large-amplitude Alfvén waves in open and closed coronal structures: A numerical study, *J. Geophys. Res.*, *107*(A11), 1380, doi:10.1029/2001JA005062, 2002.

Groth, C. P. T., D. L. De Zeeuw, T. I. Gombosi, and K. G. Powell, Global three-dimensional MHD simulation of a space weather event: CME formation, interplanetary propagation, and interaction with the magnetosphere, *J. Geophys. Res.*, *105*(A11), 25,053–25,078, 2000.

Guhathakurta, M., and R. Fisher, Solar wind consequences of a coronal hole density profile: Spartan 201-03 coronograph and Ulysses observations from 1.15 $R_\odot$ to 4 AU, *Astrophys. J.*, *499*, L215–L218, 1998.

Guhathakurta, M., A. Fludra, S. E. Gibson, D. Biesecker, and R. Fisher, Physical properties of a coronal hole from a coronal diagnostic spectrometer, Mauna Loa Coronograph, and LASCO observations during the Whole Sun Month, *J. Geophys. Res.*, *104*(A5), 9801–9808, 1999.

Hassler, D. M., G. J. Rottman, E. C. Shoub, and T. E. Holzer, Line broadening of Mg × ΛΛ609 and 625 coronal emission lines observed above the solar limb, *Astrophys. J.*, *348*, L77–L80, 1990.

Hollweg, J. V., Some physical processes in the solar wind, *Rev. Geophys.*, *16*(4), 689–720, 1978.

Hollweg, J. V., On WKB expansions for Alfvén waves in the solar wind, *J. Geophys. Res.*, *95*(A9), 14,873–14,879, 1990.

Hollweg, J. V., and P. A. Isenberg, Generation of the fast solar wind: A review with emphasis on the resonant cyclotron interaction, *J. Geophys. Res.*, *107*(A7), 1147, doi:10.1029/2001JA000270, 2002.

Hundhausen, A. J., *Coronal Expansion and Solar Wind*, 329 pp., Springer-Verlag, New York, 1972.

Jacques, S. A., Momentum and energy transport by waves in the solar atmosphere and solar wind, *Astrophys. J.*, *215*, 942–951, 1977.

Jacques, S. A., Solar wind models with Alfvén waves, *Astrophys. J.*, *226*, 632–649, 1978.

Levine, R. H., M. D. Altschuler, and J. W. Harvey, Solar sources of the interplanetary magnetic field and solar wind, *J. Geophys. Res.*, *82*(7), 1061–1065, 1977.

Lionello, R., J. A. Linker, and Z. Mikić, Including the transition region in models of the large-scale solar corona, *Astrophys. J.*, *546*, 542–551, 2001.

MacCormack, R. W., Numerical solution of the interaction of a shock wave with a laminar boundary layer, in *Proceedings of the Second International Conference on Numerical Methods in Fluid Dynamics*, *Lect. Notes Phys.*, vol. 8, edited by M. Holt, pp. 151–163, Springer-Verlag, New York, 1971.

Mikić, Z., and J. A. Linker, The large-scale structure of the solar corona and inner heliosphere, in *Solar Wind Eight*, edited by D. Winterhalter et al., pp. 104–107, AIP Press, Woodbury, N.Y., 1996.

Mikić, Z., J. A. Linker, D. D. Schnack, R. Lionello, and A. Tarditi, Magnetohydrodynamic modeling of the global solar corona, *Phys. Plasmas*, *6*(5), 2217–2224, 1999.

Munro, R. H., and B. V. Jackson, Physical properties of a polar coronal hole from 2 to 5 $R_\odot$, *Astrophys. J.*, *213*, 874–886, 1977.

Ofman, L., and J. M. Davila, Alfvén wave heating of coronal holes and the relation to the high-speed solar wind, *J. Geophys. Res.*, *100*(A12), 23,413–23,425, 1995.

Ofman, L., and J. M. Davila, Solar wind acceleration by large-amplitude nonlinear waves: Parametric study, *J. Geophys. Res.*, *103*(A10), 23,677–23,690, 1998.

Osherovich, V. A., I. Tsur, and E. B. Gliner, Theoretical model of the solar corona during sunspot minimum. I. Quasi-static approximation, *Astrophys. J.*, *284*, 412–421, 1984.

Phillips, J. L., et al., Ulysses solar wind plasma observations from pole to pole, *Geophys. Res. Lett.*, *22*(23), 3301–3304, 1995.

Pizzo, V., A three-dimensional model of corotating streams in the solar wind: 3. Magnetohydrodynamic streams, *J. Geophys. Res.*, *87*(A6), 4374–4394, 1982.

Pizzo, V. J., The evolution of corotating stream fronts near the ecliptic plane in the inner solar system: 2. Three-dimensional tilted-dipole fronts, *J. Geophys. Res.*, *96*(A4), 5405–5420, 1991.

Pneuman, G. W., and R. A. Kopp, Gas-magnetic field interactions in the solar corona, *Sol. Phys.*, *18*, 258–270, 1971.

Riley, P., J. A. Linker, and Z. Mikić, An empirically driven global MHD model of the solar corona and inner heliosphere, *J. Geophys. Res.*, *106*(A8), 15,889–15,901, 2001.

Roberts, D. A., Interplanetary observational constraints on Alfvén wave acceleration of the solar wind, *J. Geophys. Res.*, *94*(A6), 6899–6905, 1989.

Ruderman, M. S., M. L. Goldstein, D. A. Roberts, A. Deane, and L. Ofman, Alfvén wave phase mixing driven by velocity shear in two-dimensional open magnetic configurations, *J. Geophys. Res.*, *104*(A8), 17,057–17,068, 1999.

Saito, K., M. Makita, K. Nishi, and S. Hata, A non-spherical axisymmetric model of the solar K corona of the minimum type, *Ann. Tokyo Astron. Obs., 2nd ser.*, *12*(2), 51–173, 1970.

Sittler, E. C., Jr., and M. Guhathakurta, Semi-empirical two-dimensional magnetohydrodynamic model of the solar corona and interplanetary medium, *Astrophys. J.*, *523*, 812–826, 1999.

Smith, E. J., A. Balogh, M. Neugebauer, and D. McComas, Ulysses observations of Alfvén waves in the southern and northern solar hemispheres, *Geophys. Res. Lett.*, *22*(23), 3381–3384, 1995a.

Smith, E. J., A. Balogh, M. E. Burton, G. Erdös, and R. J. Forsyth, Results of the Ulysses fast latitude scan: Magnetic field observations, *Geophys. Res. Lett.*, *22*(23), 3325–3328, 1995b.

Smith, E. J., A. Balogh, R. F. Forsyth, B. T. Tsurutani, and R. P. Lepping, Recent observations of the heliospheric magnetic field at Ulysses: Return to low latitude, *Adv. Space Res.*, *26*(5), 823–832, 2000.

Steinolfson, R. S., S. T. Suess, and S. T. Wu, The steady global corona, *Astrophys. J.*, *255*, 730–742, 1982.

Stewart, G. A., and S. Bravo, Latitudinal solar wind velocity variations from polar coronal holes: A self-consistent MHD model, *J. Geophys. Res.*, *102*(A6), 11,263–11,272, 1997.

Suess, S. T., and E. J. Smith, Latitudinal dependence of the radial IMF component: Coronal imprint, *Geophys. Res. Lett.*, *23*(22), 3267–3270, 1996.

Suess, S. T., A. K. Richter, C. R. Winge, and S. F. Nerney, Solar polar coronal hole—A mathematical simulation, *Astrophys. J.*, *217*, 296–305, 1977.

Suess, S. T., A.-H. Wang, S. T. Wu, G. Poletto, and D. J. McComas, A two-fluid, MHD coronal model, *J. Geophys. Res.*, *104*(A3), 4697–4708, 1999.

Tóth, G., The $\nabla \cdot \mathbf{B} = 0$ constraint in shock-capturing magnetohydrodynamics codes, *J. Comput. Phys.*, *161*, 605–652, 2000.

Tóth, G., and D. Odstrčil, Comparison of some flux corrected transport and total variation diminishing numerical schemes for hydrodynamic and magnetohydrodynamic problems, *J. Comput. Phys.*, *128*, 82–100, 1996.

Totten, T. L., J. W. Freeman, and S. Arya, An empirical determination of the polytropic index for the free-streaming solar wind using Helios 1 data, *J. Geophys. Res.*, *100*(A1), 13–17, 1995.

Usmanov, A. V., A global numerical 3-D MHD model of the solar wind, *Sol. Phys.*, *146*, 377–396, 1993a.

Usmanov, A. V., The global structure of the solar wind in June 1991, *Sol. Phys.*, *148*, 371–382, 1993b.

Usmanov, A. V., and M. Dryer, A global 3-D simulation of interplanetary dynamics in June 1991, *Sol. Phys.*, *159*, 347–370, 1995.

Usmanov, A. V., M. L. Goldstein, B. P. Besser, and J. M. Fritzer, A global MHD solar wind model with WKB Alfvén waves: Comparison with Ulysses data, *J. Geophys. Res.*, *105*(A6), 12,675–12,695, 2000.

Wang, A.-H., S. T. Wu, S. T. Suess, and G. Poletto, Global model of the corona with heat and momentum addition, *J. Geophys. Res.*, *103*(A2), 1913–1922, 1998.

Wang, Y.-M., Flux-tube divergence, coronal heating, and the solar wind, *Astrophys. J.*, *410*, L123–L126, 1993.

Wang, Y.-M., and N. R. Sheely Jr., Solar wind speed and coronal flux-tube expansion, *Astrophys. J.*, *355*, 726–732, 1990.

Wang, Y.-M., N. R. Sheeley Jr., J. L. Phillips, and B. E. Goldstein, Solar wind stream interactions and the wind speed-expansion factor relationship, *Astrophys. J.*, *488*, L51–L54, 1997.

Winterhalter, D., E. J. Smith, M. E. Burton, N. Murphy, and D. J. McComas, The heliospheric plasma sheet, *J. Geophys. Res.*, *99*(A4), 6667–6680, 1994.

Zhao, X., and J. T. Hoeksema, The temporal evolution of the radial component of the heliospheric magnetic field, in *Solar Wind 8*, edited by D. Winterhalter et al., pp. 494–497, AIP Press, Woodbury, N.Y., 1996.

M. L. Goldstein and A. V. Usmanov, Code 692, NASA Goddard Space Flight Center, Greenbelt, MD 20771, USA. (melvyn.goldstein@gsfc.nasa.gov; usmanov@geo.phys.spbu.ru)